Low-frequency waves in the Santa Barbara Channel observed by high-frequency radar

Edwin Beckenbach and Libe Washburn

Institute for Computational Earth System Science, Department of Geography, University of California, Santa Barbara, Santa Barbara, California, USA

Received 10 June 2003; revised 20 October 2003; accepted 11 November 2003; published 13 February 2004.

[1] Three years of high-frequency radar observations in the Santa Barbara Channel reveal sequences of alternating cyclonic and anticyclonic vortices propagating westward with a period of approximately 2 weeks. The sequences last up to a few months and occur intermittently throughout the year. The velocity distributions of cyclones and anticyclones are antisymmetric with a mean propagation speed of $\sim$5 km d^{-1} and relative vorticity of order 0.1 *f*. Complex empirical orthogonal function decomposition in the 10–20 day passband partitions variance into two dominant modes. The first mode represents the vortices with an average period of 14.4 days. The second mode represents alongshore fluctuations with an average period of 13.3 days. Amplitude functions of the two modes correlate with in situ current time series at 5 and 45 m depths obtained from moorings at the east and west channel entrances, suggesting coupling with the larger-scale circulation of the northern Southern California Bight. The observations support interpretation of mode 2 as a coastal trapped wave since the period and alongshore flow are consistent with previous observations and predictions. We hypothesize that mode 1 is a resonant response of the Santa Barbara Basin in the form of a trapped topographic Rossby mode. The spatial mode resembles the predicted pattern based on a simplified analytical model of the fundamental mode. The amplitude of mode 1 is consistently large when the frequencies of modes 1 and 2 converge, suggesting that the vortices are a basin-scale resonant response to coastal trapped waves. *INDEX TERMS:* 4520 Oceanography: Physical: Eddies and mesoscale processes; 4512 Oceanography: Physical: Currents; 4508 Oceanography: Physical: Coriolis effects; 4516 Oceanography: Physical: Eastern boundary currents; 4544 Oceanography: Physical: Internal and inertial waves; *KEYWORDS:* propagating eddies, Santa Barbara Channel, coastal trapped waves

Citation: Beckenbach, E., and L. Washburn (2004), Low-frequency waves in the Santa Barbara Channel observed by high-frequency radar, *J. Geophys. Res.*, *109*, C02010, doi:10.1029/2003JC001999.

1. Introduction

[2] The coastal ocean supports diverse circulation patterns due to the imposition of the coastal boundary and sloping topography. Along straight coastlines, coastal upwelling [*Sverdrup*, 1938] and coastally trapped waves (CTWs) including barotropic Kelvin and topographic Rossby modes are well known examples with straightforward analytical descriptions [*Brink*, 1991]. Real coastlines can be irregular with complex offshore topography and, in the presence of stratification, three-dimensional fluid structures are common including jets, eddies, fronts and a series of baroclinic Kelvin and Rossby waves. The Santa Barbara Channel (SBC) is an example of a coastal region with variable bottom slope, offshore islands, and a deep basin, the Santa Barbara Basin (SBB). The SBC, located at the northern end of the Southern California Bight (SCB), runs east to west approximately 100 km between Pt. Mugu and Pt. Conception. The Northern Channel Islands of Anacapa, Santa Cruz, Santa Rosa and San Miguel form the Channel's southern boundary. The 40 km wide channel is a region where coastal circulation patterns are complicated by irregular topography, interacting water masses and strong wind stress forcing.

[3] Circulation patterns in the SBC were first assessed by *Kolpack* [1971] on the basis of hydrographic surveys conducted during 1969 and 1970 in response to the Santa Barbara Channel oil spill of 1969. Drifter cards released during these surveys revealed that a complex field of eddies prevailed in the eastern channel, positioned between a large persistent cyclonic cell in the western channel and northwest flow at the eastern entrance. Later research conducted during the Organization of Persistent Upwelling Systems (OPUS) project and the Santa Barbara Channel Circulation Study (1983–1984) examined local flow patterns in response to the frequent, vigorous wind forcing common in the western channel. *Brink* [1983], *Huyer* [1983] and *Winant et al.* [1987] found that near Pt. Conception and to the north flow responds to alongshore wind stress following classical Ekman dynamics and the thermal wind relationship. In contrast, *Atkinson et al.* [1986], *Barth and Brink*

0148-0227/04/2003JC001999$09.00

[1987] and *Brink and Muench* [1986] described flow within the SBC as a complex system of eddies, jets, and fronts with poor correlation to local wind forcing. More recently, several studies have described flow in the SBC as a sequence of synoptic states consisting of upwelling/relaxation and cyclonic regimes regulated through a momentum balance including significant contributions from wind stress, wind stress curl, sea level tilt and Coriolis terms [*Auad and Henderschott*, 1997; *Harms and Winant*, 1998; *Oey*, 1999; *Oey et al.*, 2001; *Winant et al.*, 1999].

[4] An additional circulation pattern observed by *Harms and Winant* [1998] within the SBC is that of "propagating cyclones". They observed that AVHRR satellite images often indicate cyclonic eddies drifting westward with a period of approximately 14 days. As one cyclonic eddy approached the western entrance, another appeared north of the western tip of Santa Cruz Island. These features extended below the thermocline based on observation from an array of vector measuring current meters (VMCMs) at depths of 5 and 45 m placed around the SBB. Within the 10–25 day band, maximum lagged correlations of longitudinal velocities between neighboring stations indicated a translation rate of 0.06 m s^{-1}.

[5] *Auad and Henderschott* [1997] and *Auad et al.* [1999] investigated mechanisms of current generation and volume transport at the eastern entrance of the SBC in the 6–18 day band. They found significant linear relationships between transport and both local wind stress and remote adjusted sea level (ASL). Regional-scale ASL behavior was consistent with theoretical predictions of a poleward propagating hybrid Kelvin-topographic Rossby wave [*Brink and Chapman*, 1985]. Their mass transport time series for the east and west entrances and the interisland passages of the SBC also exhibited energy peaks at periods near 14 days.

[6] In this study, propagating flow features in the 10–20 day band, comparable to the bands identified by *Auad and Henderschott* [1997] and *Harms and Winant* [1998] are further explored. The features propagate westward but not because of the planetary beta effect; rather, we argue that the propagation direction results from the orientation of the bottom slope in the SBC. Using high-frequency (HF) radar with coverage over SBB, we have isolated the surface expression of what we hypothesize is a low-frequency resonant response of the basin to forcing by CTWs propagating poleward along coast of the Southern California Bight (SCB). The resonant response resembles a barotropic trapped Rossby mode (TRM) similar to the TRMs identified in the Straits of Sicily [*Pierini*, 1996] and on the Iceland-Faeroe Ridge [*Miller et al.*, 1996].

[7] The propagating eddy patterns within the 10–20 day band do not dominate circulation within the channel, but represent ~15% of the subtidal velocity variance. However, these patterns are a curious aspect of the local circulation which may affect other flow regimes. For example, the propagating eddy patterns appear to constructively and destructively interfere with a persistent cyclonic circulation found over the SBB that can retain juvenile fishes [*Nishimoto and Washburn*, 2002]. In addition, the regions between eddy centers are alternating cross-channel jets, which propagate westward along with the vortices and may significantly influence cross-channel advection between the mainland coast and the offshore islands.

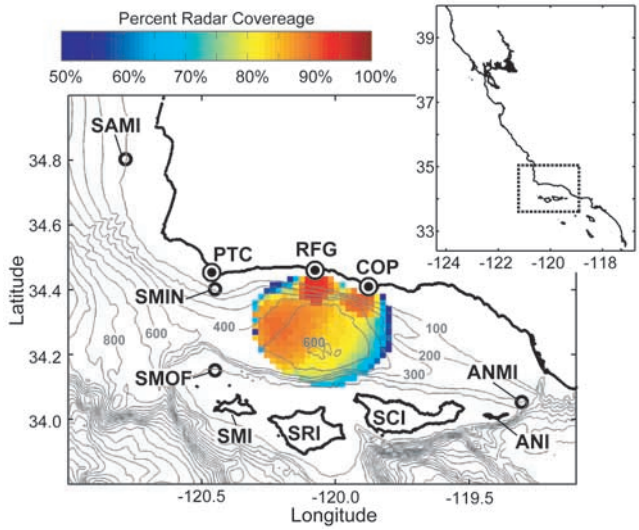

Figure 1. Study area showing the Santa Barbara Channel and Santa Barbara Basin. Color contours show percent coverage from the HF radar array over the 3 year study period. HF radar locations at Point Conception (PTC), Refugio (RFG), and Coal Oil Point (COP) are indicated by dots in circles. SAMI, SMIN, SMOF, and AMNI are current meters deployed by the CCS. SMI, SRI, SCI, and AMNI identify San Miguel, Santa Rosa, Santa Cruz, and Anacapa Islands, respectively.

[8] A discussion of the observational setting including the HF radar network and four nearby moorings follows in section 2. The methods used in processing and interpretation of the data are explained in section 3. Flow kinematics based on assessment of the data in the 10–20 day band and resulting circulation patterns are detailed in section 4. An interpretation of flow patterns based on a simple analytical model is discussed in section 5. Conclusions are given in section 6.

2. Observations

[9] Hourly surface current observations from an array of three HF radars from 1 January 1998 through 31 December 2000 are the primary data used in this study. The HF radars were direction-finding systems (Coastal Ocean Dynamics Applications Radar or CODAR, manufactured by CODAR Ocean Sensors, Ltd. of Los Altos, CA) operating at ~12 MHz over a range of 42 km with resolution of 1.5 km and azimuthal resolution of 5°. Radial current vectors were available from three radars on the mainland coast (from east to west) at Coal Oil Point (COP), Refugio State Beach (RFG), and Pt. Conception (PTC) (Figure 1). Following *Paduan and Rosenfeld* [1996], eastward and northward velocity components were computed at points over a 2 km square grid. The grid consists of 360 contiguous points covering 1440 km^2 centered over the SBB. Surface current vectors are calculated from all radial vectors within 3 km of each grid point using the least squares method of *Gurgel* [1994].

[10] We subjectively determined the coverage area by attempting to maximize the size of the long-term foot print of the HF radar array while minimizing data gaps. Grid

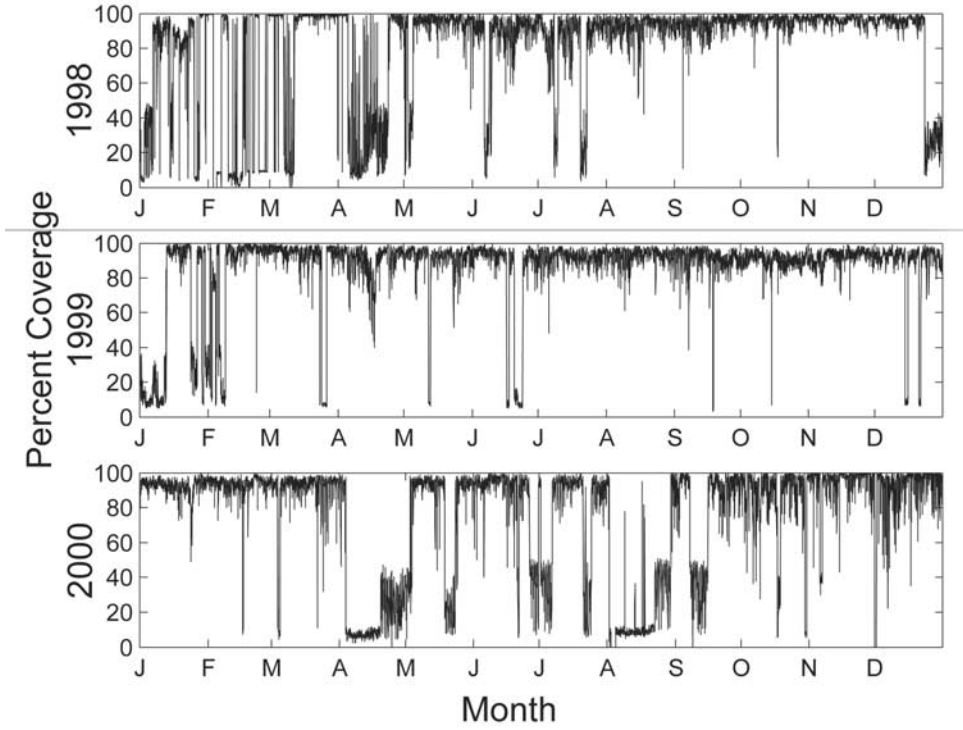

Figure 2. Percent of spatial coverage for the study area as a function of time. Percent coverage is the hourly percentage of grid cells within the radar footprint (Figure 1) returning velocity observations.

points were excluded within 3 km of the coastline to avoid contamination from overland signal returns and avoid the radar baselines. As described by B. Emery et al. (Evaluating CODAR high frequency radars for measuring surface currents: Observations in the Santa Barbara Channel, submitted to *Journal of Atmospheric and Oceanic Technology*, 2000), spatial coverage from each site within the radar footprint varied over a range of timescales because of several factors, including failure of the radar algorithms to determine radial currents, broadcast interference, ionospheric propagation, and equipment failures (Figure 2). Surface current vectors are available for a minimum of 50% and maximum of 95% of the 3 year record at individual grid points (color contours, Figure 1). Averaged over all grid points, the velocity time series over the coverage area is 80% populated. Because our analysis focused on timescales greater than 10 days, only the longer lasting gaps were a major concern in the analysis. Fortunately, these were infrequent in the record, particularly in 1998 and 1999, occurring only in mid-December 1998 to mid-January 1999, April 2000, and mid-August to mid-September 2000.

[11] Data from long-term moorings, maintained by the Center for Coastal Studies (CCS) at the Scripps Institution of Oceanography, place the higher spatial resolution HF radar observations in a larger spatial context and provide subsurface observations. Four moorings (Anacapa Middle, ANMI; San Miguel Inshore, SMIN; San Miguel Offshore, SMOF; and Point Sal Middle, SAMI) with vector measuring current meters (VMCMs) at 5m and 45m depths provided velocity measurements every 4 min at the east and west entrances and north of Pt. Conception (Figure 1). Hourly, quality-controlled data were made available to us by CCS. Data concurrent with the HF radar time series were available through 19 November 1999 and 13 August 2000 for the 45 and 5 mVMCMs, respectively. *Harms and Winant* [1998], *Hendershott and Winant* [1996] and *Chen and Wang* [1999] describe the mooring data in detail.

3. Methods

[12] We used several data processing steps to characterize narrowband wave-like circulation patterns. Data gaps were filled, the frequency band containing the wave-like motions was identified, and the time series were filtered. The time series were then decimated to one observation per day.

[13] Relative vorticity ζ proved useful in quantifying the propagating vortices because of their strong rotation. We computed hourly estimates of ζ at grid points using centered first differences at points inside the coverage footprint (i.e., only at points where total velocity vectors were available at the four adjacent points). ζ estimates were normalized relative to planetary vorticity f ($8.2 \times 10^{-5}\mathrm{s}^{-1}$ at 34.25°N).

[14] Some basic characteristics of the propagating vortices, such as length scales and period, were determined by examining the filtered time series. Then complex empirical orthogonal function (CEOF) decomposition was used to quantify the strength of the dominant flow patterns. Stream function estimates of the dominant modes were used for flow visualization and for comparison of the propagating vortices with an analytical TRM model.

3.1. Missing Data

[15] Gaps occurred in all of the time series: 19.5% were missing over the 3 year record of HF radar data; 12.6% were missing for the 5 m moored current data records; and 13.2%

were missing for the 45m moored records. Because some of the time series analysis methods employed, such as digital filtering and CEOF decomposition, required complete time series, it was necessary to estimate missing portions of the data records. We assumed (and verified) that the velocity observations were sampled from a multivariate normal distribution. Missing observations were optimally estimated using maximum likelihood principles as described by *Orchard and Woodbury* [1972] and *Beale and Little* [1975].

[16] This method is a two-step, iterative multiple linear regression procedure. One step is parameter estimation of the data's underlying probability distribution conditioned on the observed data and the prior estimates of the missing data. The other step updates estimates of missing values by regression on the observed values using the estimated distribution parameters, in this case the mean vector and covariance matrix. The procedure starts on either step with some sensible initial estimates of the missing values or the distribution parameters and continues until convergence within a chosen tolerance is met. Algorithm details are presented in Appendix A.

3.2. Frequency Band Selection and Filtering

[17] Previous studies of low-frequency flow in the SBC have focused on the 10–25 day band [*Harms and Winant*, 1998] and the 6–18 day band [*Auad and Henderschott*, 1997]. We identified westward propagating features within the overlapping 10–20 day band by computing the squared coherence γ^2 for time series of ζ along the SBC axis as discussed below in section 4. To further examine the flow in this band, we digitally filtered the surface current time series in two steps using MATLAB numerical routines. The two-step filtering process was necessary because the passband frequency range (0.05–0.1 cycle per day, cpd) was a small fraction (1/600th) of the total bandwidth (0–12 cpd). First, a fifth order Butterworth low-pass filter with a half-power cutoff corresponding to a 36 hr period was applied to the hourly velocity time series and the data were decimated to one point per day. Second, the decimated data were band-pass filtered to retain periods between 10 and 20 days using a ninth order Type II Chebyshev filter with ripple peaks of −40 db relative to the passband. Both filters were applied in the forward and reverse directions to eliminate phase shifts.

3.3. Complex Empirical Orthogonal Function Analysis

[18] Once the current time series were filtered to eliminate variance outside of the 10–20 day band, we computed complex empirical orthogonal functions (CEOFs) following the method of *Wallace* [1972] to evaluate the spatial patterns and temporal evolution of the dominant modes of variability. *Auad and Henderschott* [1997] used the technique to examine low-frequency coastal waves propagating through the SBC based on moored current and bottom pressure time series. They also present a succinct description of the method. In the CEOF procedure each time series (u and v are treated independently as scalars) is augmented with an imaginary component to provide phase information to enable detection of variance propagation through the array. For example,

$$V(x_m, t) = v(x_m, t) + iH[v(x_m, t)], \tag{1}$$

where H[$v(x_m, t)$] is the Hilbert transform of $v(x_m, t)$, x_m is the mth grid location, and t is time. The time series of V are then represented by expansions like

$$V(x_m, t) = \sum_{i=1}^{M} A_i(t) B_i(x_m) = \sum_{i=1}^{M} |A_i(t)||B_i(x_m)| e^{i\left[\varphi_{A_i}(t) + \varphi_{B_i}(x_m)\right]}, \tag{2}$$

where, $A_i(t)$ is the complex temporal amplitude function, $B_i(x_m)$ is the complex spatial mode or eigenvector, and φ_{A_j} and φ_{B_j} are the phase functions corresponding to $A_i(t)$ and $B_i(x_m)$. φ_{A_j} and φ_{B_j} describe the propagation characteristics of the ith mode. CEOFs differ from the more conventional real EOFs because the associated eigenvalue problem is based on the band-averaged cross-spectrum matrix rather than the standard data covariance matrix. With real EOFs propagating features can be spread across several modes, obscuring their detection. With narrow-banded CEOFs, propagating modes are distinct and uncorrelated across a finite frequency band. We argue that the two dominant CEOFs found in the 10–20 day band represent distinct propagating waves, although no such dynamical interpretation is implied by the CEOF method, which is purely statistical.

3.4. Stream Function Estimation

[19] We use stream functions Ψ to estimate dynamic topography associated with surface flow patterns and to compare these results with a simple theoretical model. An estimate of the nondivergent flow field, recovered by differentiation of the stream function, is a useful first-order characterization of the circulation patterns. The residual velocity fields contain the corresponding divergent component of circulation.

[20] We computed Ψ using harmonic expansions as described by *Cho et al.* [1998] and *Vastano and Reid* [1985]. The expansions were estimated by minimization of the square of the difference in the u (eastward) and v (northward) velocity components between velocity observations and nondivergent velocities based on the derivatives of Ψ. A similar method was used by *Vastano and Reid* [1985] with two-dimensional (2-D) half-range sine expansions with constant Ψ on the domain boundaries. *Cho et al.* [1998] used the approach on a boundary-fitted orthogonal coordinate system for arbitrary Ψ along open lateral boundaries with explicit boundary conditions imposed for the alongshore boundaries. When open boundaries circumscribe the domain, as in our analysis, 2-D Fourier basis functions with arbitrary phase can be used to avoid edge constraints as shown in Appendix B. Stream function contours are scaled as $\eta = \Psi f/g$ to represent equivalent variation in dynamic height.

4. Results

4.1. Propagating Rotary Flows

[21] Preliminary analysis of raw hourly surface current patterns from the HF radars revealed westward propagating rotary flow patterns such as those shown in Figure 3. The example shows two oppositely rotating eddy-like patterns over the Santa Barbara Basin on 26 May 1999. The cyclonic flow pattern on the western boundary of the basin is intensified on its western, southward flowing side with

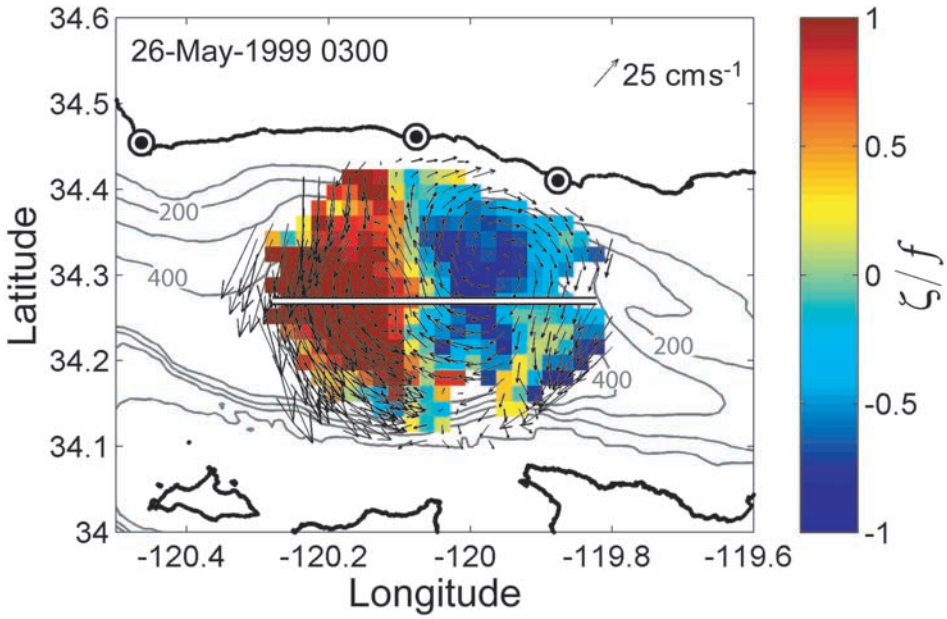

Figure 3. Two counterrotating eddies over the Santa Barbara Basin on 16 May 1999 at 0300 GMT. Color contours give ζ/f according to the color scale to the right. The white line identifies the transect used to produce the time-longitude contours of Figures 4, 6, 7a, and 12a.

maximum flow speeds of $\sim$0.5 m s^{-1} and ζ/f of order 1. The anticyclonic pattern on the northeast side of the basin has lower flow speeds, is more symmetric, and has ζ/f of order -0.6. Both patterns span the north-south extent of the basin with horizontal length scales on the order of the basin width or about 25 km. Sequences of images suggested a westward propagation speed of about 4.7 km d^{-1}. Similar propagating flow patterns at comparable speeds have been found in other circulation studies of the SBC. For example, *Harms and Winant* [1998, Plate 1a] show a westward propagating cyclonic eddy visualized by a sequence of satellite sea surface (SST) images in August 1994.

[22] Typically, energetic flow patterns in the SBC obscure propagating rotary structures like those of Figure 3. One such pattern is the mean tendency for cyclonic flow in the western SBC as discussed by *Harms and Winant* [1998], *Hendershott and Winant* [1996], *Atkinson et al.* [1986], *Auad et al.* [1999], and *Brink and Muench* [1986]. From these HF radar observations we estimate a mean ζ for the 3 year record of $0.18f$ over the radar coverage area shown in Figure 1; maximum observed values averaged over the coverage area are on the order of $0.5f$. Local values exceeding f are observed occasionally as in Figure 3. Often propagating eddies appear as modulations of the larger cyclonic flow pattern: propagating cyclones temporarily intensify the pattern, propagating anticyclones weaken it.

[23] Time-longitude contours for 1999 (Figure 4a) show the evolution of ζ/f along an east-west transect down the channel axis (transect shown in Figure 3) calculated using the filled-in hourly time series with no filtering. Coherent rotational features, mostly cyclonic, at scales approaching the basin width appear as continuous, nearly vertical bands. The dashed vertical line of Figure 4 identifies the time of the vortex pattern of Figure 3. The flow varies on timescales of days to weeks over the basin, but a tendency for cyclonic flow (red-biased contours) is evident. Periods of negative vorticity (blue-biased contours) lasting up to a few weeks also occur, particularly along the transect's eastern portion. A general negative sloping of the contours indicates persistent westward propagation of cyclonic and anticylonic vorticity features along the SBC axis. Low-pass filtering of the time series (cutoff frequency of 1/36 hr^{-1}) more clearly shows the westward propagation by removing variance at tidal and higher frequencies (Figure 4b) It also clarifies the occurrence of negative vorticity, particularly on the eastern portion of the transect.

[24] To identify the dominant timescales associated with westward propagation, we computed the squared coherence, γ^2, and phase difference, ϕ between vorticity time series at the transect endpoints. A peak in γ^2 between 0.05–0.1 cpd indicates significant coherence (95% confidence threshold) for periods of 10–20 days (Figure 5). The γ^2 peak of 0.5 corresponds to a period of approximately 15 days. ϕ in the 10–20 day band ranges from 195°–240° with the peak corresponding to 210°. The positive ϕ of 210° indicates that vorticity at the east end of the transect leads the west end by about 9 days, consistent with the westward propagation inferred from Figure 4. The distance between the ends is 42 km so the implied westward propagation speed is $\sim$4.7 km d^{-1}.

[25] On the basis of the γ^2 peak, velocity data were band-pass filtered (section 3.2) to remove variance outside the 10–20 day passband. Contours of ζ/f in the passband show distinct alternating stripes which represent trains of counter-rotating features (Figure 4c). This banding suggests a channel-scale instability or wave phenomenon. The correspondence between the red and blue stripes and propagating cyclonic and anticyclonic vortices is apparent when the

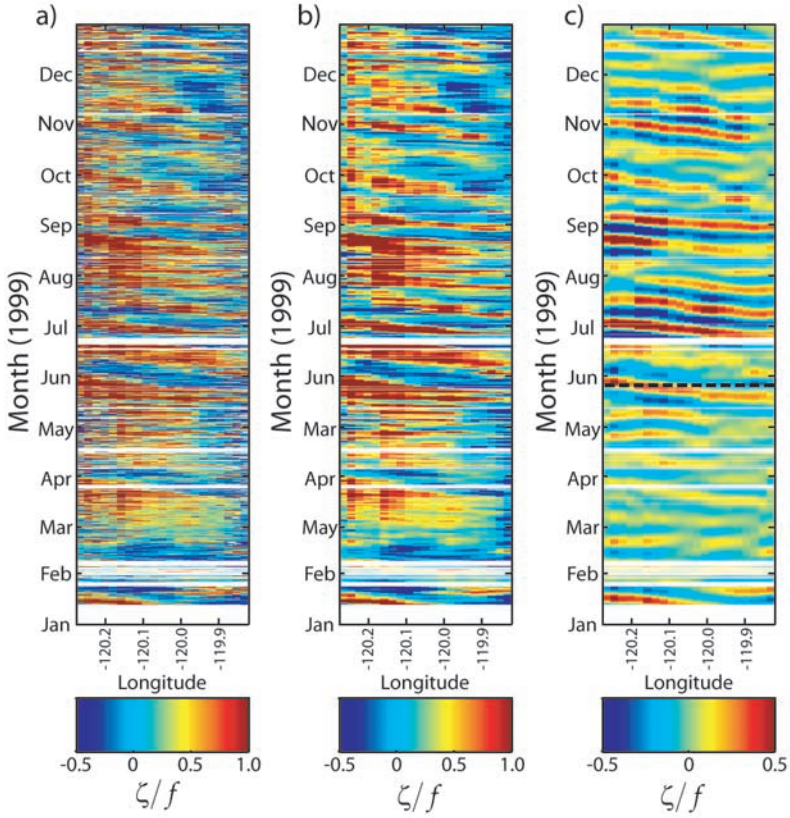

Figure 4. (a) Time-longitude contours of ζ/f computed from hourly HF radar observations along transect shown in Figure 3 for 1999. (b) As in Figure 4a but with ζ/f low-pass filtered with a cutoff frequency of 1/36 hr^{-1}. (c) As in Figure 4a but with ζ/f band-pass filtered with cutoff frequencies 1/10 to 1/20 d^{-1}. Dashed vertical line indicates time of velocity pattern of Figure 3. Color scales indicate values of ζ/f.

stripes are compared with patterns of band-pass-filtered velocity vectors (Figure 6). During the period 21 June to 21 July 1999 alternating anticyclonic and cyclonic vortices move through the coverage area. The propagating pattern varies strongly but recurs over the 3 year record with the vortex trains lasting up to several months, as from July through September 1999 (Figure 4c).

[26] Vorticity time series along the transect reveal that the radar footprint is often too small for observing the complete evolution of the propagating features. Some of the stripes in Figure 4c are cut off at both ends, although this occurs more frequently at the west end of the transect. There are no periods during which the HF radar coverage extended farther east so investigation into an eastward origin is precluded. During May–October 1998 coverage extended an additional 12 km to 120.4°W, over the western sill of the basin. We used data from this area to examine the evolution of the vortices as they propagate over the sill. Other periods of continuous coverage over this area were too short for analysis at periods of 10–20 days.

[27] ζ/f contours over the extended coverage area show a marked decrease in relative vorticity as the vortices propagate westward over the western sill (Figure 7a). Some propagating variance in the 10–20 day band persists over the sill such as in late June and early July 1998. Shading of the contours indicates that the largest values of ζ/f are found

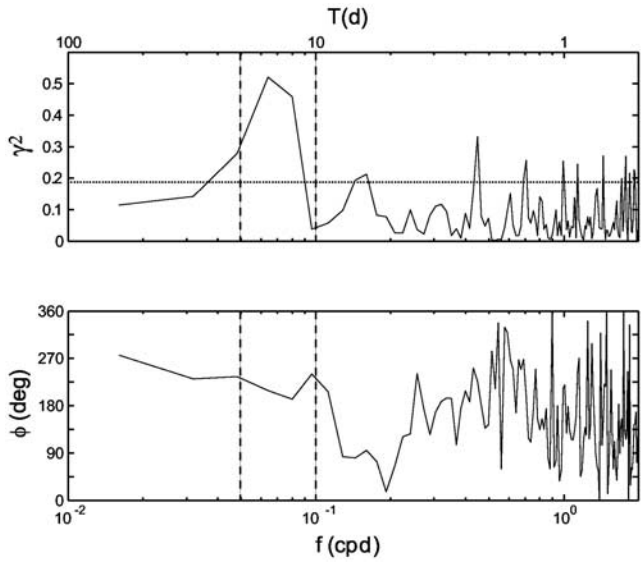

Figure 5. (a) Squared coherence γ^2 and (b) phase ϕ of ζ between the ends of the transect shown in Figure 3. Dashed lines indicate the frequency band 1/10 to 1/20 d^{-1} over which γ^2 is significant. The dotted line shows the 95% significance threshold for γ^2.

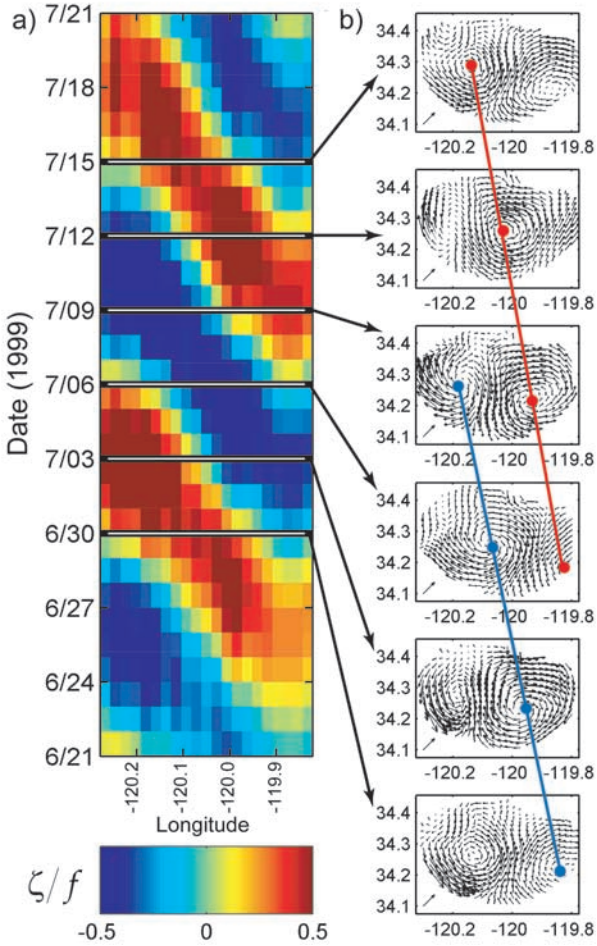

Figure 6. (a) Longitude-time contours of ζ/f for 21 June to 21 July 1999. Color scale for the contours is given at the bottom. (b) Surface velocity patterns at 3 day intervals as indicated by horizontal lines in Figure 6a. The sloping red (blue) line connects centers of cyclones (anticyclones). Arrow at lower left in each velocity pattern indicates 10 cm s^{-1}. All data have been band-pass filtered to retain frequencies from 1/10 to 1/20 d^{-1}.

near 120.2°W, above the slope leading to the western sill. Then the amplitude of ζ/f fluctuations decreases rapidly over the upper slope and remains small over the sill. This is confirmed in a comparison of the average envelope of ζ/f and the bathymetric profile along 34.27°N (dashed line, Figure 7b). The amplitude envelope of ζ/f averaged over the 15 June to 15 August 1998 interval, shown by the dotted bars in Figure 7a, increases from 0.11 on the eastern end of the coverage area to a peak of 0.55 at 120.17° W. West of the peak it decreases rapidly to about 0.15 over the sill itself. A similar reduction in ζ/f amplitude at the ends of the transect were indicated for the entire 3 year record but the trend was not as well resolved because of the limited westward extent of the transect.

[28] The pattern of striped contours in Figure 7a and the eddy velocity patterns of Figure 6b suggest symmetry between the cyclonic and anticyclonic features. We quantified this symmetry by conditionally averaging numerous cyclones together and numerous anticyclones together at similar phases during their propagation. To estimate the velocity field of the propagating cyclones, all times over the 3 year band-pass-filtered record were identified which had maxima of $\zeta/f > 0.2$ at a point near the center of the SBB (circle, Figure 8a). A total of 32 maxima satisfied this condition. At these times fully developed cyclones occupied the central portion of the basin. Then for each grid point at these times the velocity components, u and v, were individually averaged. The resulting pattern is shown as black arrows in Figure 8a. A similar procedure for anticyclones found 35 peaks with $\zeta/f < -0.2$. Velocity components $-u$ and $-v$ for the anticyclones are shown as gray arrows in Figure 8a. Together these cyclones and anticyclones account for the upper 45% of $|\zeta/f|$ for the 3 year record. Strong spatial correlation among the vectors ($\rho = -0.998$; $r^2 = 0.995$) indicates the high degree of antisymmetry between the mean velocity fields of the cyclones and anticyclones over most of the coverage area. Large differences in current direction only occur over the western sill where velocity vectors are small.

[29] Because of the symmetry between the cyclones and anticyclones and their radial similarity, we computed representative radial profiles of tangential velocity, v_t (r), and radial velocity, v_r (r), where r is the distance from the center of the velocity patterns (plus signs (+) in Figures 8a and 8b).

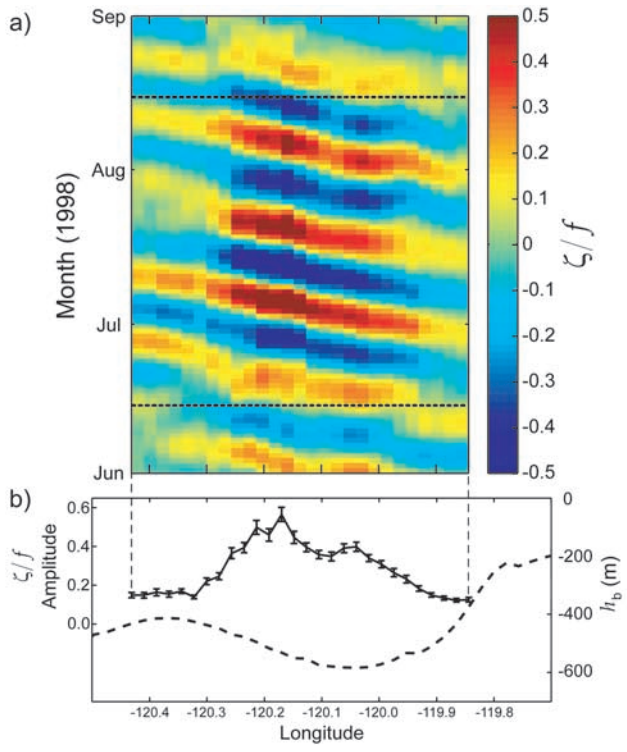

Figure 7. (a) Longitude-time contours of ζ/f for 1 June to 1 September 1998 along the extended transect (see text). The color scale for ζ/f is given at right. (b) Solid line (left scale) shows the average profile of the amplitude envelope of ζ/f along the extended transect from 15 June to 15 August 1998. This time period is indicated by the dotted lines in Figure 7a. Dashed line (right scale) shows bottom depth along the transect direction of Figure 3.

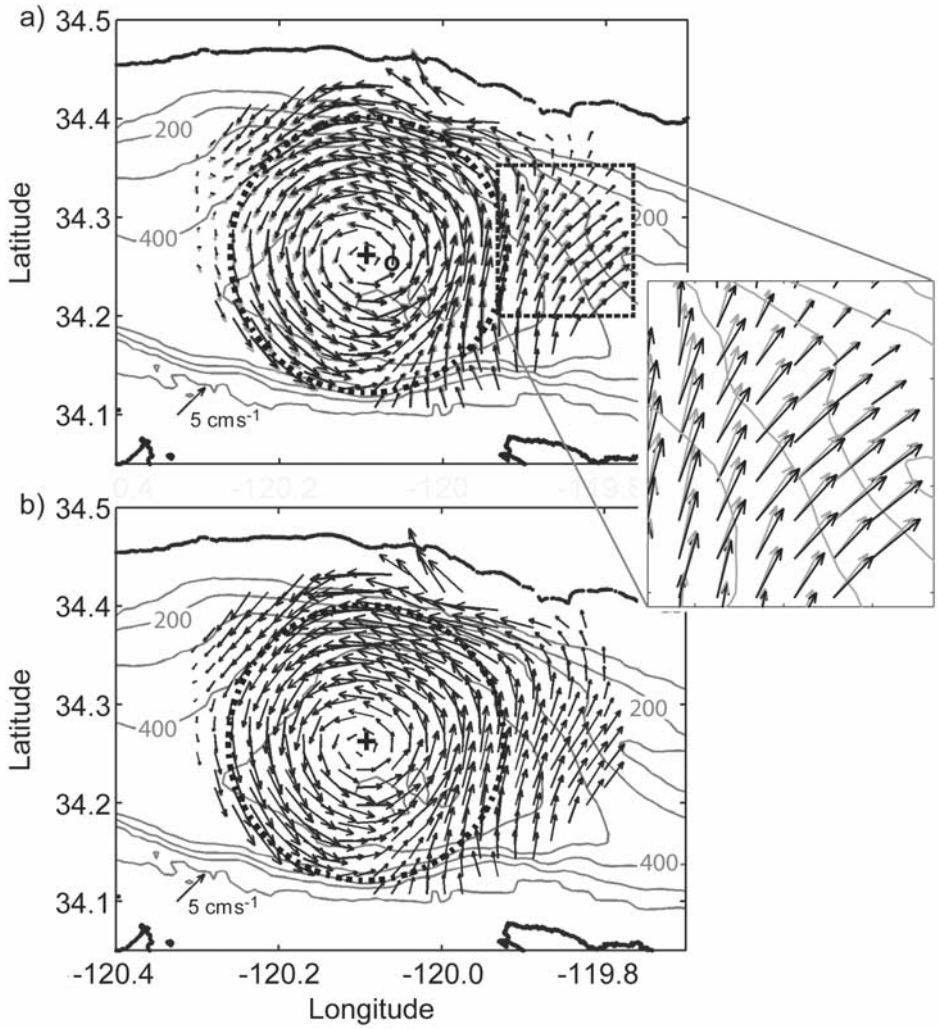

Figure 8. (a) Black arrows show the conditionally averaged cyclonic velocity pattern, and shaded arrows show the conditionally averaged anticyclonic velocity pattern. Velocity components of anticyclonic pattern have been multiplied by -1 for comparison. Patterns are formed by averaging velocity fields together subject to the conditions: (1) local maxima (for cyclones) and minima (for anticyclones) occur at the location indicated by the black circle, and (2) these maxima and minima satisfy $|\zeta|/f > 0.2$. Velocity scale is at lower left. The enlarged panel details the high correlation between the black and shaded arrows. (b) Cyclonic velocity pattern from CEOF mode 1 for phase $\varphi_{A_j} = 221°$. In both Figures 8a and 8b, dotted circle indicates area, with center at plus sign, used to produce the radial distributions of Figure 9.

We used the mean velocity patterns of Figure 8a with cyclones combined with anticyclones scaled by -1.

[30] Using Stoke's theorem and the divergence theorem applied to a circular area R with perimeter C,

$$v_t(r) = \frac{1}{2\pi r} \oint_{C(r)} \vec{v} \cdot \hat{T} ds = \frac{1}{2\pi r} \iint_{R(r)} \nabla \times \vec{v} dA \tag{3}$$

$$v_r(r) = \frac{1}{2\pi r} \oint_{C(r)} \vec{v} \cdot \hat{n} ds = \frac{1}{2\pi r} \iint_{R(r)} \nabla \cdot \vec{v} dA, \tag{4}$$

where $\hat{T}$ and $\hat{n}$ are unit vectors tangent and normal to C. v_t (r) and v_r (r) were calculated by integrating $\nabla \times \vec{v}$ and $\nabla \cdot \vec{v}$ (from central differences) over concentric circles with radii from 2 to 16 km at 2 km intervals (dashed lines, Figures 9a and 9b). The circles were centered on the mean eddy center (plus (+) sign, Figure 8a).

[31] We also computed the radial ζ(r) and $\nabla_h \cdot \vec{v}(r)$ profiles by applying the curl and divergence operators in cylindrical coordinates to v_t (r) and v_r (r),

$$\frac{\zeta(r)}{f} = \frac{1}{f} \nabla \times \vec{v} = \frac{1}{rf} \frac{\partial}{\partial r}(r v_t) \tag{5}$$

$$\nabla_h \cdot \vec{v}(r) = \frac{1}{r} \frac{\partial}{\partial r}(r v_r). \tag{6}$$

These equations were evaluated using centered differences of the appropriate velocity profiles from radii of 1 km to

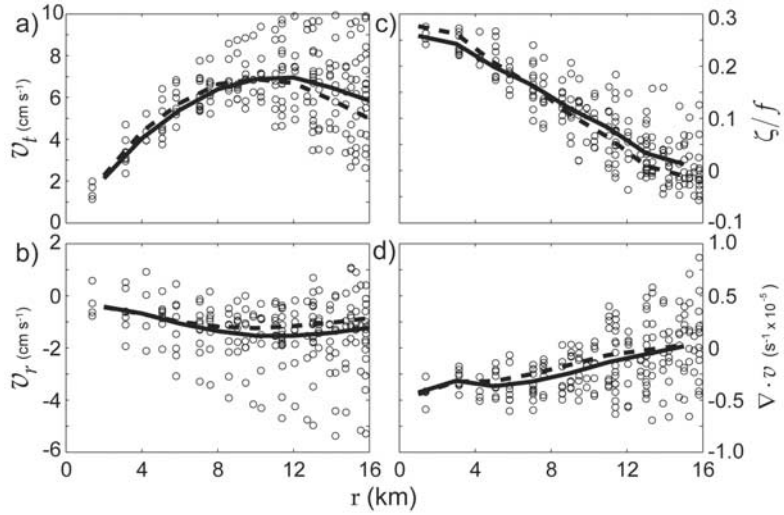

Figure 9. Mean radial distributions of (a) tangential velocity, $\vec{v}_t(r)$, (b) radial velocity, $v_r(r)$, (c) normalized vorticity, ζ/f, and (d) divergence, $\nabla_h \cdot \vec{v}(r)$. Solid lines are averages based on conditionally averaged patterns of Figure 8a, and dashed lines are based on CEOF mode 1 pattern of Figure 8b. Scatter about the profiles are point calculations based on the CEOF mode 1 pattern. The scatter represents variability arising because of departure of the mean distribution from radial symmetry.

15 km at 2 km intervals (dashed lines, Figures 9c and 9d). Tangential and radial velocities at the eddy center were assumed to be zero.

[32] Profiles of v_t (r) and v_r (r) are linearly related (r^2 = 0.97), increasing from zero at the eddy center (extrapolating) to maximal values at ~10 km (Figures 9a and 9b). Signs are opposite with positive v_t (r), representing cyclonic circulation, associated with negative v_r (r), representing convergent flow toward the eddy center. The profile of v_t (r) increases from ~2 cm s^{-1} at 2 km radius to a maximum of ~7 cm s^{-1} at 10 km before decreasing to 5–6 cm s^{-1} at 16 km (Figure 9a). The v_r (r) profile is negative everywhere, lying in the range −0.5 to −1.5 cm s^{-1} (Figure 9b). Radial profiles of $\zeta(r)/f$, and $\nabla_h \cdot \vec{v}$ (r) are similarly related (Figures 9c and 9d). Extreme values of opposite sign, 0.28 for $\zeta(r)/f$ and -4.1×10^{-6} s^{-1} for $\nabla_h \cdot \vec{v}$ (r), occur at the cyclone center and transition monotonically toward zero at 16 km, on the outer edge. Anticyclonic flow (negative $v_t(r)$ and $\zeta(r)/f$) is associated with divergence (positive v_r (r) and $\nabla_h \cdot \vec{v}(r)$) and is represented by scaling the radial profiles of Figure 9 by a factor of −1.

4.2. Modes of Variance Over the Santa Barbara Basin

[33] Time-longitude contours of ζ/f (Figure 4) and the time series of velocity distributions (Figure 6) suggest that trains of westward propagating cyclones and anticyclones are common over the SBB. We employed CEOFs to isolate two modes of propagating variance associated with the timescales of these motions and then explored the relationship between the modes.

[34] The first two CEOF modes account for 45% and 20% the velocity variance in the 10–20 day band, respectively. The spatial structure of mode 1 is similar to the trains of cyclones and anticyclones as is seen by comparing the mean velocity field of the cyclones (Figure 8a) with the velocity field of mode 1 at phase angle φ_{A_j} = 221° (Figure 8b). Westward propagation of cyclones and anticyclones over the SBB is evident over one complete cycle of mode 1 as shown in Figure 10a. As φ_{A_j} progresses from 0 through π/2, an anticyclonic eddy translates westward and a cyclonic eddy enters the eastern edge of the coverage. At π the cyclonic eddy occupies the center of the basin; only a hint of the original anticyclonic eddy remains to the west. This sequence resembles the time series of velocity patterns of Figure 6b. Stream function distributions scaled as η (Figure 11a) indicate that the propagating eddies span the basin. Accompanying sea surface elevation differences between centers of the cyclones and anticyclones are on the order of 5 mm over separation distances of approximately 30 km.

[35] A strong correspondence exists between ζ/f in the 10–20 day band (Figure 12a) and $|A_1(t)|$ (black line, Figure 12b) over the 3 year record. Gaps in coverage appear as white vertical bands in Figure 12a. Curves of $|A_1(t)|$ and $|A_2(t)|$ are continuous in Figure 12b because data were filled using the technique described in section 3. Large peaks in $|A_1|$ occur from June 1998 through January 1999 and from June through August 1999 (Figure 4c) when striped vorticity contours are prominent. Mode 1 is relatively weak in winter and early spring 1998 and 1999 and throughout 2000. φ_{A_1} increases steadily over the record with an average frequency $\langle f_1 \rangle$ = 0.069 ± 0.010 cpd corresponding to an average period of T_1 = 14.3 d (Figure 12c) with the given frequency envelope representing ±1 standard deviation of the instantaneous frequency.

[36] Mode 2, accounting for 20% of variance, exhibits a broad pattern of along-channel velocity fluctuations with much lower ζ than mode 1 (Figure 10b). $|A_2|$ does not show any distinct seasonal trend and is typically smaller than $|A_1|$ (Figure 12b). Flow for mode 2 is generally eastward and northeastward when φ_{A_2} = 0 and westward and southwestward when φ_{A_2} = π. Mode 2 has a slightly higher frequency than mode 1 with $\langle f_2 \rangle$ = 0.075 ± 0.015 cpd and mean period T_2 = 13.3 d. The mode 2 stream function is a broad pattern of tilting η contours which run diagonally across

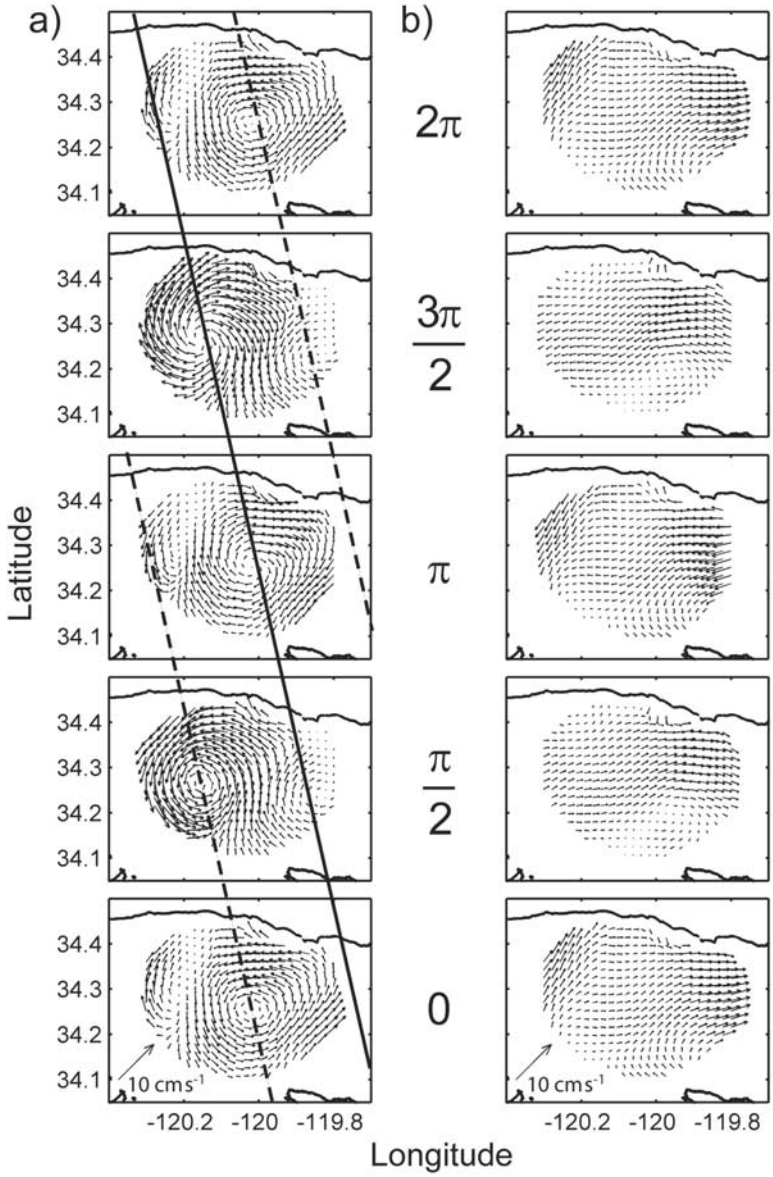

Figure 10. (a) Velocity patterns of CEOF mode 1 at values of phase φ_{A_j} shown at left of each panel. Sloping solid (dashed) lines connect centers of cyclones (anticyclones). Velocity scale is at lower left in bottom panel. (b) As in Figure 10a but for CEOF mode 2.

the channel from southwest to northeast (Figure 11b). Along the shelf on the northern boundary of the basin they run approximately parallel to isobaths. Further south they cross isobaths. The maximum change in η across the center of the basin is $\sim$ 5 mm. Crowding of η contours indicate highest flow speeds over the northeastern portion of the basin. Spreading η contours over the southwestern region indicates a broadening and weakening flow. Turning of contours near Santa Cruz Island when φ_{A_2} = 0 and π suggests that flow along the island coast is opposite that along the mainland.

[37] Although modes 1 and 2 explain 45% and 20% of the total velocity variance in the 10–20 day band, respectively, their spatial distributions are biased such that the modes contribute over 60% of total variance in the regions where each dominates. The spatial distribution of variance indicates that mode 1 explains most of the variance over the basin and the steep slope on the northern edge of the basin (Figure 13a) while mode 2 explains most of the variance in the northeastern portion of the basin (Figure 13b). Combined, the modes explain the most variance, 60–80%, over the northern slope of the basin and the least, 20–40%, along the southern slope (Figure 13c).

[38] Frequency variability based on standard deviations is large compared with differences between the average values of f_1 and f_2 such that the individual frequency envelopes overlap. Coupling between modes 1 and 2 is suggested by time series of $|A_1|$ and the absolute value of the frequency difference $|\Delta f\,(t)| = |f_2\,(t) - \langle f_1 \rangle|$ (Figure 14). When $|\Delta f|$ is small and exhibits local minima, such as in early December

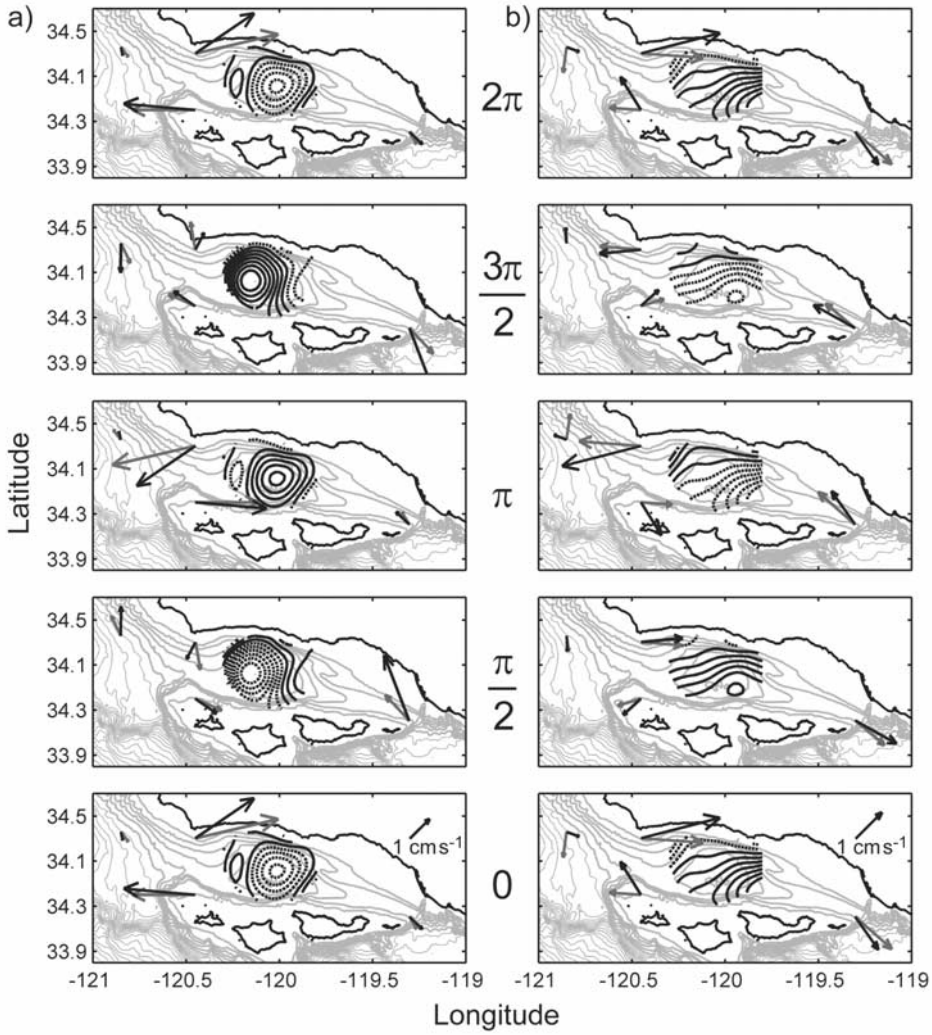

Figure 11. (a) Stream function for CEOF mode 1 corresponding to velocity patterns of Figure 10a. (b) As in Figure 11a but for CEOF mode 2. Contours indicate sea surface height differences with a contour interval of 0.5 mm. Dashed contours are negative. Black and shaded vectors show correlated velocities (see text) at 5 and 45 m, respectively, from CCS moorings. Velocity scales are shown on bottom panels. Current vectors at westernmost current meter shown (SAMI) are displaced south of the actual mooring location. Figure 1 shows all mooring locations.

1998, late March and early July 1999, $|A_1|$ is large and exhibits local maxima. Conversely, when $|\Delta f|$ exhibits local maxima, such as in mid-November 1998, the end of March and mid-June 1999, $|A_1|$ exhibits local minima. This temporal pattern occurs consistently over the 3 year record, although the amplitudes of maxima and minima in $|A_1|$ are not related to $|\Delta f|$ in a simple linear way. For example, the peak in $|A_1|$ at the beginning of December 1998 is higher than the peak of early January 1999, even though its $|\Delta f|$ is larger. Similarly, the trough in $|A_1|$ in late March 1999 is slightly deeper than the trough of mid-June 1999, even though its $|\Delta f|$ is much smaller.

[39] The mean velocity distribution for the cyclonic eddy in Figure 8a is similar to the first CEOF mode at $\varphi_{A_1} = 221°$ as shown in Figure 8b. This CEOF distribution was used as the basis for recalculating radial profiles for comparison with those derived from conditional averages. A strength of the CEOF decomposition is the implicit incorporation within each complex mode of the entire time series. Averaging at a single phase angle depends on the continuity of the propagating pattern at all phase angles over all times. In addition, no arbitrary constraints on vorticity magnitude, such as the vorticity threshold used in the conditional averages of Figure 8, are required to extract the dominant velocity distributions.

[40] Radial distributions of v_t (r), v_r (r), $\zeta(r)/f$, and $\nabla_h \cdot \vec{v}(r)$ computed from mode 1 are similar to those computed from the mean flow patterns of (Figure 8a). Profiles from mode 1 (solid lines, Figure 9) correspond to a phase angle of 221° where the correlation with the mean pattern of Figure 8 was greatest ($r^2 = 0.96$). To produce mean profiles from mode 1, its (nondimensional) spatial pattern was multiplied by the average magnitude of the upper 45% of values of its temporally varying amplitude func-

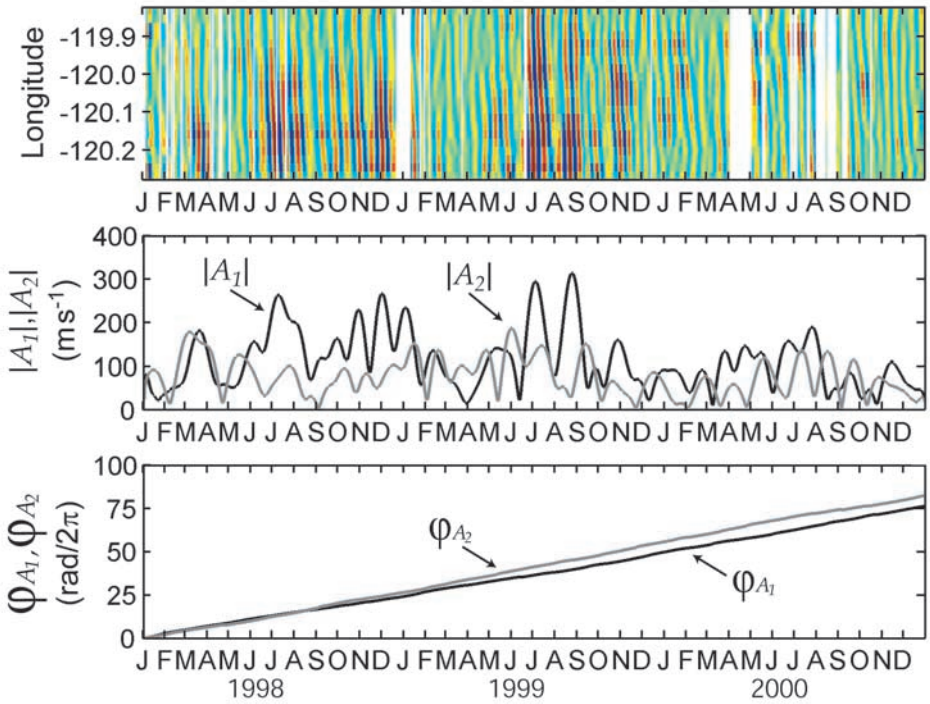

Figure 12. (a) Time-longitude contours for 1998–2000 of ζ/f band-pass filtered with cutoff frequencies 1/10 to 1/20 d^{-1}. Color scale as in Figure 4c. (b) Time series of CEOF amplitude functions $|A_1|$ (black line) and $|A_2|$ (shaded line). (c) As in Figure 12b but for CEOF phase functions φ_{A_j} (black line) and φ_{A_2} (shaded line).

tion. The threshold of 45% was chosen to match the upper 45% of $|\zeta/f|$ values used in calculating the mean velocity distribution.

[41] To show variability about the mean radial distributions due to departures from radial symmetry, panels of Figure 9 include values of each variable at individual grid points as a function of radius based on the CEOF distribution scaling as described above. Scatter in the radial distributions is large, particularly for v_r (r) and $\nabla_h \cdot \vec{v}(r)$, although even with the wide range most v_r (r) and $\nabla_h \cdot \vec{v}(r)$ values are negative.

[42] Propagating vortices occur over a wide range of intensity as shown by time series of $|A_1|$ (Figure 12b). A convenient approach to quantifying the range of feature properties is to use the distribution of $|A_1|$ as an index. Cumulative percentile values of $|A_1|$ specify corresponding values of v_t (r), v_r (r), $\zeta(r)/f$, and $\nabla_h \cdot \vec{v}$ (r) (Table 1). v_t (r) and v_r (r) are computed at a radius of 10 km where they are largest. For $\zeta(r)/f$ and $\nabla h \cdot \vec{v}$ (r), which are largest at the eddy center, the nearest calculated values at 1 km radius values are given. Values of Table 1 are for the cyclonic eddy as represented by the first spatial mode at $\varphi_{A_1} = 221°$. A representative anticyclonic eddy followed by an additional phase of π results in values of equal magnitude and opposite sign. Taking the median (50th percentile) of $|A_1|$ as an example, corresponding values of v_t (r) and v_r (r) at 10 km radius are 4 cm s^{-1} and -0.9 cm s^{-1}, respectively. Maximum values (100th percentile) for the 3 year record are 12.8 cm s^{-1} and -2.8 cm s^{-1}. The ratio of v_r (r) to v_t (r) is approximately 0.20. Median values for $\zeta(r)/f$ and $\nabla_h \cdot \vec{v}$ (r) at 1 km radius are 0.15 and -2.52×10^{-6} s^{-1}, respectively, and maximum values are 0.48 and -7.9×10^{-6} s^{-1}.

4.3. Larger-Scale Current Patterns

[43] To explore possible connections between surface flow patterns over the SBB and larger-scale coastal flows we examined the correlation between the CEOF modes and velocity time series from the CCS moorings at the east and west channel entrances. The mooring data were not incorporated into the CEOF analysis because they only overlapped with the HF radar time series for 23 to 32 months. Instead the mooring data were related to the CEOF modes using complex linear regression of the mooring data on the amplitude functions A_1 and A_2. Consistent with the HF radar data, the mooring data were band-pass filtered and augmented with their Hilbert transforms. Then complex regression coefficients and associated r^2 values were calculated.

[44] The resulting moored current patterns are included with the CEOF stream functions in Figure 11. Currents at SAMI are displaced from their actual position for comparison with the HF radar-derived stream functions. Correspondence between the CEOF modes and correlated mooring patterns is seen for the most widely spaced currents at ANMI and SAMI, suggesting that both spatial modes 1 and 2 are related to oscillations of the large-scale alongshore coastal flow, especially to the south but also to the north of Pt. Conception.

[45] The sense of the correlated moored currents agrees with the CEOF spatial distributions. The portion of the currents at ANMI correlated with mode 1 are out of phase with those at SMIN; maximum currents at ANMI occur

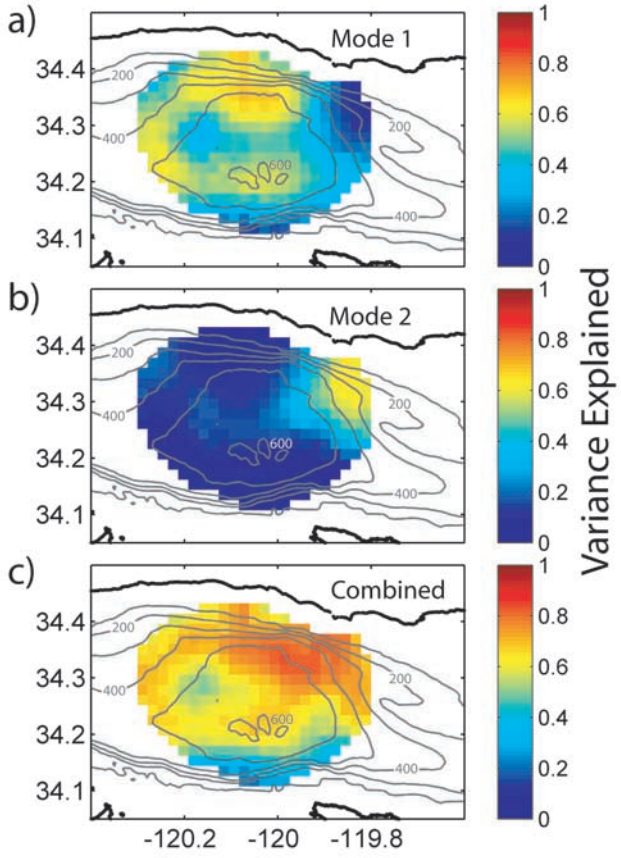

Figure 13. Spatial distributions of the fraction of variance explained by (a) mode 1, (b) mode 2, and (c) combined modes 1 and 2.

simultaneously with minimum currents at SMIN and vice versa (Figure 11a). In contrast, the second mode agrees with ANMI and SMIN in direction and magnitude as may be seen by comparing Figures 10b and 11b. These characteristics suggest that the mode 1 circulation pattern is smaller

Table 1. Representative Eddy Parameters as Functions of the Percentile of $|A_1|$[a]

A_1, Percentile	v_t (r), cm s^{-1}	v_r (r), cm s^{-1}	ζ/f	$\nabla_h \cdot \vec{v}$ (r), s^{-1}
10th	1.7	−0.4	0.06	−1.0
25th	2.5	−0.5	0.09	−1.5
50th	4.1	−0.9	0.15	−2.5
75th	6.0	−1.3	0.22	−3.7
90th	8.5	−1.9	0.32	−5.2
100th	12.8	−2.8	0.48	−7.9

[a]Maximum v_t (r) and v_r (r) at a radius of 10 km and maximum ζ/f and $\nabla_h \cdot \vec{v}(r)$ at a radius of 1 km from the eddy center are shown.

than the mooring array while the mode 2 pattern is larger. At SMIN and SMOF the alongshore velocity components are approximately opposite in direction with comparable magnitudes. Their phase is consistent with propagation of the weakening (mode 1) eddy patterns over the western sill. With respect to mode 2 (Figure 11b), flow at SMOF is opposite but reduced in magnitude compared with SMIN. This corresponds well with the reversing of flow seen just north of the Channel Islands, at the southern edge of the HF radar coverage and the expected offshore attenuation in amplitude associated with CTWs.

[46] The portions of mooring variance in the 10–20 day band explained by A_1 and A_2 are given by r^2 in Table 2. For the four moorings, the average variance explained at 5 and 45 m is 18.5% and 22.7%, respectively for A_1 and 9.2% and 13.4% for A_2. The most significant relationships are with moorings located in the channel (ANMI, SMIN, and SMOF), particularly with those closest to the coverage area (SMIN and SMOF), where between 31% and 43% of the mooring velocity variances are explained by A_1 and A_2 combined. The least significant relationships are seen at the most remote mooring SAMI where 9% to 22% of the variance is explained. The relationships are more significant at the channel entrances with A_1 and A_2 explaining approximately 30–40% of the mooring velocity variances. In all cases, A_1 and A_2 combined explain more variance at 45 m than at 5 m. For the second mode the strongest correlations

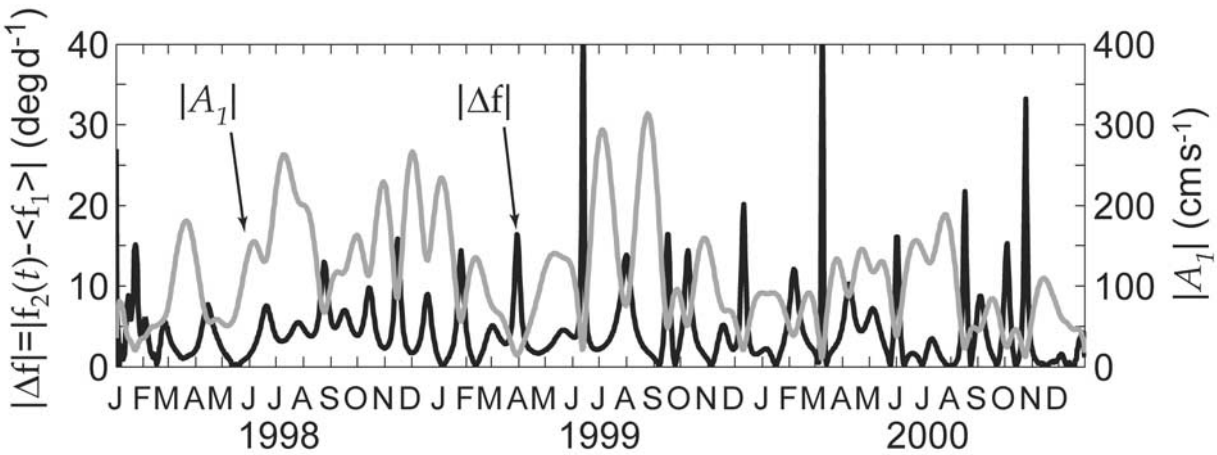

Figure 14. Time series for 1998–2000 of frequency difference magnitude $|\Delta f|$ (black line) and magnitude $|A_1|$ of CEOF mode 1 (shaded line).

Table 2. Variance of Moored Currents at 5 and 45 m Explained by the Complex Amplitude Functions

	Variance Explained, %		
Depth	A_1	A_2	Combined
	SAMI		
5 m	7.1	2.0	9.1
45 m	11.6	10.2	21.8
	SMIN		
5 m	19.7	19.0	38.7
45 m	30.2	13.1	43.3
	SMOF		
5 m	26.2	6.0	32.2
45 m	35.7	7.3	43.1
	ANMI		
5 m	21.2	9.9	31.1
45 m	13.5	22.8	36.3

are found along the mainland coast (ANMI and SMIN). This agrees with the interpretation of the first mode as a basin response and the second as a coastal-trapped wave.

5. Discussion

[47] Evolving patterns of surface currents in the SBC in the 10–20 day band suggests a basin-scale (~30 km) modification of the larger-scale coastal flow associated with poleward-propagating CTWs with wavelengths much larger than the channel scale. Previous studies have shown that CTWs commonly occur along the west coast of North America, including the SCB and around Pt. Conception [*Auad and Henderschott*, 1997; *Battisti and Hickey*, 1984; *Davis and Bogden*, 1989; *Hickey*, 1992]. *Auad and Henderschott* [1997] observed propagating features in the SBC in the 6–18 day band at longer-than-channel scales, which they concluded were hybrid Kelvin-Rossby waves. The second CEOF mode in this study resembles a CTW with surface currents approximately parallel to isobaths along the mainland coast and with an indication of current direction reversal along the slope north of the Northern Channel Islands (Figure 11b). *Auad and Henderschott* [1997] found good agreement between a theoretical frequency of 0.073 cpd and an observed period of 0.075 cpd. We found a period for CEOF mode 2 of 0.075 ± 0.005 cpd consistent with these values. The combination of mode 2 and correlated portion of the mooring data (Figure 11) is also consistent with a broad long-wavelength oscillating flow along the mainland coastal slope.

[48] Mode 1, representing the propagating vortices, is topographically controlled. In the meridional direction the vortices span the channel width and are limited by the steep slopes below the mainland and island shelves (Figure 11a). In the zonal direction, topographic boundaries are suggested by the decrease in vorticity amplitude over the eastern section of the basin and the western sill (Figure 7). For these motions the changes in water depth and bottom slope, and the constrictions at the open entrances to the basin appear to act as equivalent boundaries.

[49] Control of the motion by bottom topography is indicated by the Rossby wave-like characteristics of the flow including the symmetry of the cyclonic and anticyclonic patterns (Figure 8a), their westward propagation, and their frequency. The centers of the propagating vortices move westward over the basin at 4.7 km d^{-1} along the channel centerline (white dots, Figure 15a). This is consistent with topographic control in the meridional direction since the bottom shoals to the north. The path was found using a least squares fit of a quadratic surface to the mode 1 stream function for the passage of an anticyclonic eddy and then locating the surface's maximum. In addition, the spatial distribution of variance explained by mode 1 (Figure 13a) is most significant where the bottom shoals to the north and is much lower over the southern edge of the SBB where the bottom shoals to the south. Over this region the bottom slope does not allow westward propagation of topographic waves. The relationship between bottom slope, basin geometry and frequency follows.

[50] We hypothesize that the mode 1 flow pattern represents the fundamental topographic Rossby mode (TRM) of the SBB controlled by the sloping bottom. The basin has a range of bottom slopes $\partial h_B/\partial hy$ of $(6.5–9.9) \times 10^{-3}$ (subjectively estimated) between 119.0° and 120.3° (Figure 15b), where y is positive northward and h_b is bottom depth. The mean slope in the y direction is 7.2×10^{-3}. Corresponding values of the topographic β parameter

$$\beta^* = \frac{f}{D}\frac{\partial h_B}{\partial y} \tag{7}$$

are $(1.20 \pm 0.28) \times 10^{-9}$ m^{-1} s^{-1}. Here D is the depth scale (500 m). β* exceeds the planetary vorticity gradient β (2.0×10^{-11} m^{-1} s^{-1} at 34.25°) by about a factor of 100. The bottom of the basin is bounded to the north and south by steep narrow slopes descending abruptly from the coastal shelf breaks with typical β* values of 10^{-8} m^{-1} s^{-1} (Figure 15a).

[51] Characteristics of the westward propagating vortices are at least superficially consistent with the solution of TRMs in a rectangular basin as discussed by *Pedlosky* [1987] and applied by *Pierini* [1996] in the Strait of Sicily,

$$\frac{\partial}{\partial t}\nabla^2\Psi + \beta^*\frac{\partial\Psi}{\partial x} = 0. \tag{8}$$

Here Ψ is the stream function, x is positive eastward, and the bottom shoals toward positive y (north). Solution modes are of the form

$$\Psi(x,y,t) = \cos\left[\frac{\beta^* x}{2\sigma_{mn}} + \sigma_{mn}t\right]\sin m\pi\frac{x}{L_x}\sin n\pi\frac{y}{L_y}, \tag{9}$$

where L_x and L_y are the east-west and north-south basin dimensions and m and n are zonal and meridional harmonics. m and n are 1 for the fundamental mode. Use of equation (8) assumes that the ratio of the external Rossby radius $f^{-1}(gD)^{1/2}$ is large compared with the horizontal scale of the flow, the basin scales, L_x and L_y in this case [*Pedlosky*, 1987]. It further assumes that the frequencies of the wave solutions are much less than f. Both of these assumptions are well satisfied here.

[52] Solutions to the model using L_x = 50 km, L_y = 30 km, and $\beta^* = 1.20 \times 10^{-9}$ $m^{-1}s^{-1}$ (Figure 15d) are reasonably similar to the patterns of Ψ estimated from mode 1 (Figure 15c). The magnitude of the spatial component of mode 1 $|B_1(x)|$ is consistent with the product of the sines in

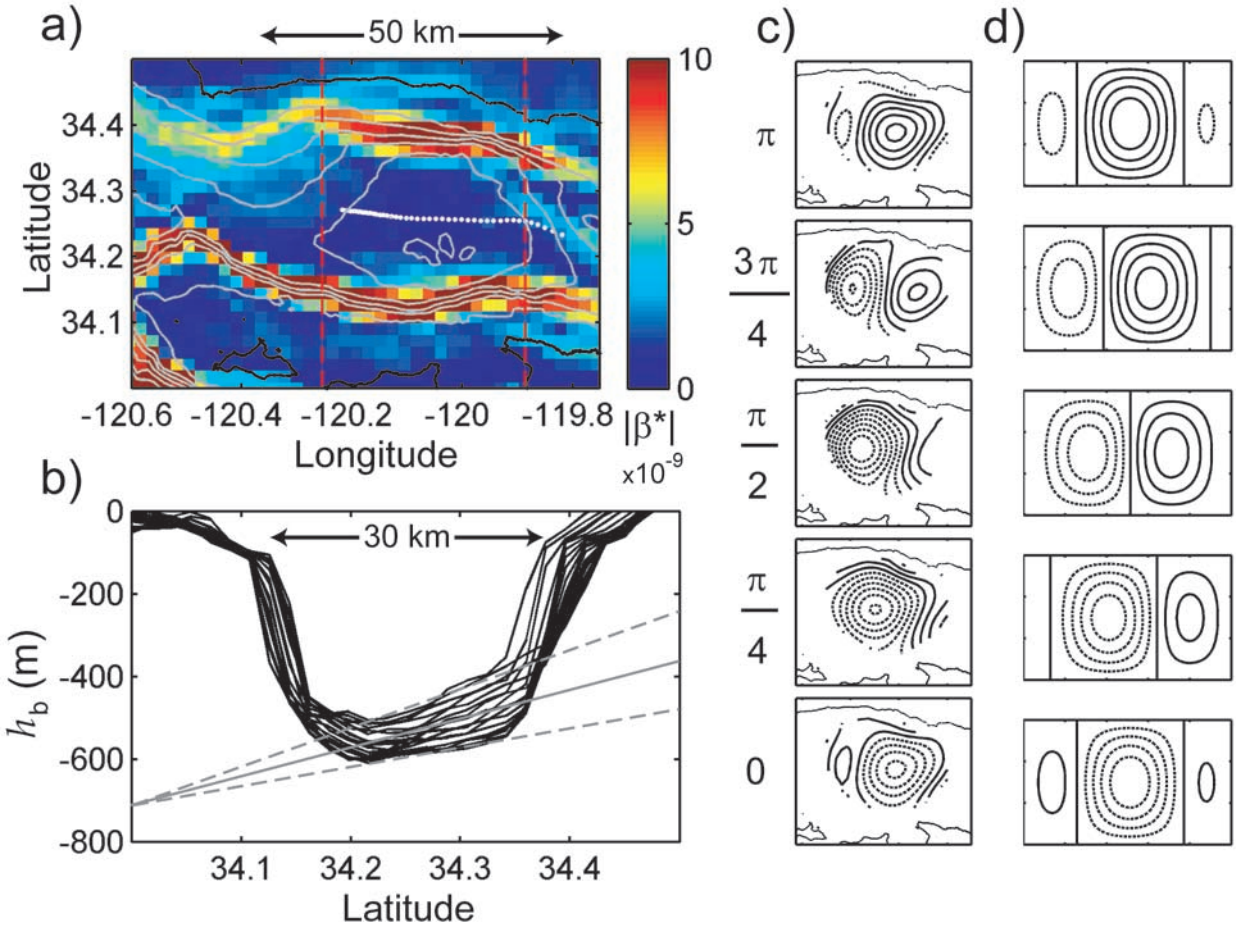

Figure 15. (a) Distribution of topographic parameter β* in western Santa Barbara Channel. White dots indicate paths of propagating eddy features based on CEOF mode 1. Cross-channel length scale (L_y = 30 km) and along-channel length scale are (L_x = 50 km) shown. (b) North-south bottom profiles across channel between longitudes indicated by vertical red dashed lines in Figure 15a. Sloping solid line shows mean bottom slope and dotted lines show range of bottom slopes estimated subjectively. (c) Stream function pattern for CEOF mode 1 for values of phase φ_{A_j} shown at left. (d) Stream function pattern for TRM model described by equation (9) for values of temporally varying phase σt shown at left. Scaling of contours is arbitrary, and negative contours are dashed.

equation (9), although the center of the pattern is shifted westward (Figures 16a and 16c). Likewise, the pattern of phase propagation for mode 1, described by $\varphi_{A_i}(t) + \varphi_{B_i}(x_m)$ is somewhat similar to the pattern of phase propagation described by the argument in square brackets (Figures 16b and 16d) in equation (9).

[53] The propagation speed of the eddy patterns and their frequency agree reasonably with the model predictions. On the basis of the model, the propagation speed c of the eddy patterns for the fundamental mode (called the carrier wave speed by *Pedlosky* [1987]) is

$$c = -\frac{2\sigma^2}{\beta^*}, \tag{10}$$

where $\sigma = \sigma_{11}$ and is the fundamental frequency. Substituting the observed frequency of mode 1, $\sigma = 2\pi[1/(14.3 \pm 2.0 \text{ days})]$ and the range of β* given above, yields c = 3.8 ± 1.4 km d^{-1}, somewhat less than the observed speed of 4.7 km d^{-1}.

[54] The frequency of the fundamental mode is

$$\sigma = -\frac{\beta^*}{\left[\left(\frac{2\pi}{L_x}\right)^2 + \left(\frac{2\pi}{L_y}\right)^2\right]^{1/2}}. \tag{11}$$

[55] Allowing for variations in basin dimensions L_x = 50 ± 10 km and L_y = 30 ± 5 km, the predicted frequency is $F = \sigma/2\pi$ = 0.068 ± 0.027 cpd which is consistent with the observed frequency of 0.070 ± 0.010 cpd. As a consistency check, if equation (11) is used to determine β* given the observed σ, L_x, and L_y (and their ranges), the resulting β* = 1.2 × 10^{-9} ± 0.3 × 10^{-9} m^{-1} s^{-1}, which agrees with estimates based on the bottom slope and Figure 15b. The

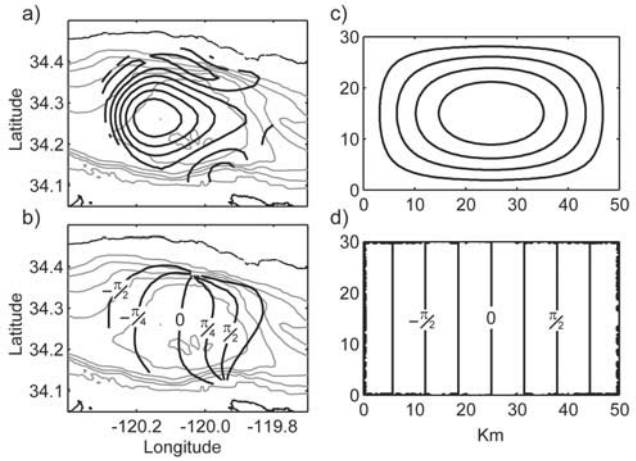

Figure 16. CEOF mode 1 shown as contours of (a) spatial amplitude $|B_1|$ and (b) spatial phase φ_{B_1} compared with (c) spatial amplitude (product of sines in equation (9)) and (d) spatial phase distribution (square bracket term in equation (9)) for TRM model.

relative contributions to variability in β^* are 25%, 23% and 52% for σ, L_x, and L_y, respectively.

[56] Figure 14 suggests that the strength of the TRM, described by $|A_1|$, is related to the frequency difference between mode 2 and the mean frequency of mode 1 $\langle f_1 \rangle$ which may represent a characteristic resonant frequency related to the basin shape. When the frequency of mode 2 approaches this resonant frequency, the TRM is sharply amplified. When the difference is large, the TRM is reduced. The relationship between the strength of the TRM and the frequency difference, however, is nonlinear. We also computed time series of the absolute value of the instantaneous frequency difference $|\Delta f'(t)| = |f_2(t) - f_1(t)|$, but found this to be much more variable and not as obviously related to $|A_1|$. This is consistent with the idea that $\langle f_1 \rangle$ is a function of the basin shape.

6. Conclusions

[57] Hourly observations of the surface circulation in the western Santa Barbara Channel were made from 1998–2000 using HF radar. Coherent, channel-scale motions were isolated within the 10–20 day band which exhibited westward propagation. Two patterns of propagating variance were identified using complex empirical orthogonal function decomposition. Mode 1, explaining 45% of the variance, is a pattern of westward propagating counterrotating vortices similar to the propagating cyclones reported by *Harms and Winant* [1998]. Mode 2, explaining 20% of the variance, is a pattern of alongshore fluctuations on the mainland coast similar to the coastal trapped waves described by *Auad and Henderschott* [1997].

[58] The propagating vortices describe by mode 1 are hypothesized to be a fundamental trapped Rossby mode of the Santa Barbara Basin. The observed stream function distribution, propagation speed (4.7 km d^{-1}) and period (14.3 days) are similar to those predicted by an analytical model [*Pedlosky*, 1987] for a barotropic trapped Rossby mode in a rectangular basin with constant bottom slope. The pattern of fluctuating along-shelf currents described by Mode 2 with a period of 13.3 days extends from the eastern entrance, through the radar coverage area, and beyond Pt. Conception indicating a long wavelength.

[59] Frequency coupling between modes 1 and 2 suggests that the propagating vortices are a resonant interaction between the basin and the coastal trapped waves. The amplitude of mode 1 consistently increases when the frequency of mode 2 and the mean frequency of mode 1 converge. The amplitude of mode 1 consistently decreases as these frequencies diverge. The relationship only exists between the frequency of mode 2 and the mean frequency of mode 1, not the instantaneous frequency, suggesting that the interaction is regulated by a constant control, assumed to be the basin geometry.

[60] The mode 1 pattern has characteristics of linear flow dynamics but a significant ageostrophic component is also present. Consistent with quasigeostrophy, the median Rossby number is 0.15 and surface convergence occurs within the cyclonic vortices and surface divergence occurs within the anticyclonic vortices. The simple linear barotropic model used for comparison does not account for these characteristics so alternative hypotheses are certainly possible. One of these is that the propagating vortices result from a baroclinic instability process. This cannot be evaluated without additional measurements of the evolving subsurface velocity and density fields in the Santa Barbara Basin. In the absence of sufficient observations, numerical simulations are an alternative approach which may shed light on the details of these flow features.

[61] These observations indicate that coastal trapped waves can interact with topographic features to produce strong secondary flows. In this case, the strong rotary flows are amplified in the basin and interact with the persistent cyclonic flow in the western Santa Barbara Channel. Similar interactions may occur more generally where basins are close enough to shore to be exposed to oscillatory flows from coastal trapped waves.

Appendix A: Missing Information Principle

[62] The missing information principle of *Orchard and Woodbury* [1972] is a theoretical framework for optimally estimating the statistical distribution parameters from incomplete data sets. Maximum likelihood estimates are used to find the distribution parameters that maximize the probability of observing the data. In the case of incomplete data the missing values are treated as additional random variables to be estimated. As a result, optimal estimates of distribution parameters and missing values are obtained simultaneously given a distribution and conditioned on the available observations. The application of the method employed for this study is detailed below.

[63] The velocity data were found to be sampled from a multivariate normal distribution and estimates were made for the distribution's mean vector and covariance matrix as well as the missing values. Simultaneous estimation is computationally prohibitive so the globally convergent iterative approach of expectation maximization (EM) is generally used [*Beale and Little*, 1975; *Jamshidian and Bentler*, 1999; *Jamshidian and Jennrich*, 1996; *Orchard and Woodbury*, 1972].

[64] The estimated data matrix $\hat{X}_k$ at time index k for p observed components is the sum of two p x 1 vectors,

$$\hat{X}_k = X_{k,o} + \hat{X}_{k,m}, \tag{A1}$$

where o and m indicate observed and estimated missing components, respectively. $X_{k,o}$ has zeros for the missing data elements; $\hat{X}_{k,m}$ has zeros for the observed data elements. $\hat{X}_{k,m}$ are estimated as expected values conditioned on the distribution's estimated mean vector, $\hat{\mu}$, covariance matrix, $\hat{\Sigma}$, and $X_{k,o}$,

$$\hat{X}_{k,m} = E\{X_{k,m}|X_{k,o}; \hat{\Sigma}, \hat{\mu}\}. \tag{A2}$$

This is equivalent to the regression of $\hat{X}_{k,m}$ on $X_{k,o}$,

$$\begin{aligned}\hat{X}_{k,m} &= \hat{\mu}_m + \hat{\Sigma}_{m,o}\hat{\Sigma}_{o,o}^{-1}(X_{k,o} - \hat{\mu}_o) \\ &= \hat{\mu}_m + (\hat{\Sigma}^{m,m})^{-1}\hat{\Sigma}^{m,o}(X_{k,o} - \hat{\mu}_o)\end{aligned}, \tag{A3}$$

where subscripts of $\hat{\Sigma}$ indicate partitions of the covariance matrix and superscripts indicate partitions of the inverted covariance matrix. For each observation the size and elements of the partitions change according to which components are observed and missing.

[65] Estimates of the distribution parameters follow

$$\hat{\mu} = \frac{1}{K}\sum_{k=1}^{K}\hat{X}_k \tag{A4}$$

$$\hat{\Sigma} = \frac{1}{K}\sum_{k=1}^{K}\left[(\hat{X}_k - \hat{\mu})(\hat{X}_k - \hat{\mu})^T + V_k\right], \tag{A5}$$

where K is the total number of observations. V_k is a bias correcting term that adjusts for the uncertainty associated with the covariance between missing values conditioned on the observed values and estimated distribution parameters,

$$V_{k,i,j} = cov(\hat{X}_{k,i}, \hat{X}_{k,j}|X_{k,o}; \hat{\mu}, \hat{\Sigma}) \tag{A6}$$

where i and j are component indices. V_k is a p x p matrix with nonzero elements only in positions involving pairs of missing observations. The partition of missing pairs for individual observations is

$$\begin{aligned}V_{m,m} &= \Sigma_{m,m} - \Sigma_{m,o}\Sigma_{o,o}^{-1}\Sigma_{o,m} \\ &= (\Sigma^{m,m})^{-1}.\end{aligned} \tag{A7}$$

[66] Computationally there is an alternation between $\hat{X}_{k,m}$ estimation and $\hat{\mu}$ and $\hat{\Sigma}$ estimation. Iteration begins with an initial guess for the unknown distribution parameters followed by estimation of the missing values using one of the forms of (A3). The choice is based on the relative number elements in $\hat{\Sigma}_{o,o}$ and $\hat{\Sigma}^{m,m}$ in order to take advantage of the smaller matrix inversion. Distribution parameters are then calculated on the basis of the completed data matrix using equation (A4) and (A5) with the bias correction of equation (A7). This process is repeated until estimates converge to within a chosen tolerance such as the convergence of successive $\hat{\Sigma}$ or $\hat{X}$ estimates.

Appendix B: Estimating the Stream Function

[67] The stream function Ψ can be approximated using a two-dimensional harmonic expansion [*Cho et al.*, 1998; *Vastano and Reid*, 1985]. When open boundaries circumscribe the domain of interest full 2-D Fourier basis functions with arbitrary phase can be used to avoid edge constraints. The series expansion of Ψ can be written as

$$\begin{aligned}\Psi(x,y) = \sum_{m=1}^{M}\sum_{n=1}^{N} &\left(A'_{mn}\cos n\alpha x + B'_{mn}\sin n\alpha x\right) \\ &\cdot \left(C'_{mn}\cos m\beta y + D'_{mn}\sin m\beta y\right),\end{aligned} \tag{B1}$$

where n and m are the number of harmonics in the x and y directions, respectively; $\alpha = \pi/L_x$ and $\beta = \pi/L_y$; L_x and L_y are the meridional and latitudinal domain scales; and A'_{mn}, B'_{mn}, C'_{mn}, and D'_{mn} are Fourier coefficients. Rewriting terms

$$\begin{aligned}\Psi(x,y) = \sum_{m=1}^{M}\sum_{n=1}^{N} &A_{mn}\cos n\alpha x\cos m\beta y + B_{mn}\cos n\alpha x\sin m\beta y \\ &+ C_{mn}\sin n\alpha x\cos m\beta y + D_{mn}\sin n\alpha x\sin m\beta y,\end{aligned} \tag{B2}$$

where A_{mn}, B_{mn}, C_{mn}, and D_{mn} are the coefficients to be determined. Nondivergent velocities are estimated from the stream function expansion

$$\begin{aligned}\tilde{u} = -\frac{\partial\Psi}{\partial y} = -\sum_{m=1}^{M}\sum_{n=1}^{N} &m\beta(-A_{mn}\cos n\alpha x\sin m\beta y \\ &+ B_{mn}\cos n\alpha x\cos m\beta y - C_{mn}\sin n\alpha x\sin m\beta y \\ &+ D_{mn}\sin n\alpha x\cos m\beta y)\end{aligned} \tag{B3}$$

$$\begin{aligned}\tilde{v} = \frac{\partial\Psi}{\partial x} = \sum_{m=1}^{M}\sum_{n=1}^{N} &n\alpha(-A_{mn}\sin n\alpha x\cos m\beta y - B_{mn}\sin n\alpha x\sin m\beta y \\ &+ C_{mn}\cos n\alpha x\cos m\beta y + D_{mn}\cos n\alpha x\sin m\beta y).\end{aligned} \tag{B4}$$

The coefficients are found by minimizing the squared residuals between the observed and estimated velocities,

$$\varepsilon^2 = \sum_{k=1}^{K}\left[(\tilde{u} - u)^2 + (\tilde{v} - v)^2\right]. \tag{B5}$$

Equations (B3) and (B4) are substituted into equation (B5) and minimization of ε^2, the RMS error, follows by setting derivatives of equation (B5), with respect to each coefficient, to zero. The resulting 4MN $\times$ 4MN linear system of equations is solved for A_{mn}, B_{mn}, C_{mn}, and D_{mn} using standard methods. Ψ, $\tilde{u}$ and $\tilde{v}$ are found by back substitution of the coefficients into equations (B2), (B3), and (B4). Additional constraints that the u and v residuals individually sum to zero can be added to force unbiased estimates of u and v.

[68] Assuming the flow to be dominantly geostrophic, Ψ is related to the dynamic topography η to within an arbitrary constant of integration C,

$$V = \frac{\partial \Psi}{\partial s} = \frac{g}{f}\frac{\partial \eta}{\partial s}, \tag{B6}$$

where f is the Coriolis parameter, g is the gravitational acceleration and s is the coordinate normal to the streamlines such that

$$\eta = \frac{f}{g}\Psi + C. \tag{B7}$$

[69] The procedure is described for a real stream function and related velocity distributions defined in two-dimensional real space, $\boldsymbol{R}^2$. Using COEFs, velocity distributions are proportional to the real part of complex eigenvectors through complex multiplication. Conveniently, the expansion is also defined for functions in two-dimensional complex space, $\boldsymbol{C}^2$. This conclusion follows from the fact that the trigonometric functions in the harmonic expansion are entire functions; the derivatives needed to define equations (B3) and (B4) and the derivatives of equation (B5) needed for minimization of residuals are continuous everywhere on the complex plane. $\boldsymbol{C}^n$ is a vector space so solution of the resulting linear system can be solved. Application of the procedure to phase-preserving complex eigenvectors results in phase-preserving complex stream function modes.

[70] **Acknowledgments.** The authors thank Brian Emery, David Salazar, and Jack Harlan for operational support and the Center for Coastal Studies at Scripps Institute of Oceanography for moored current data. EHB received support through a fellowship provided by the University of California Marine Council. The David and Lucile Packard Foundation provided operational support through a grant to the Partnership for Interdisciplinary Study of the Coastal Ocean (PISCO). Technological support came from the W.M. Keck foundation, which provided HF radar hardware, and the Environmental Technology Laboratory at NOAA, which loaned two HF radar units. The U.S. Coast guard provided site support at Point Conception, and the California Department of Recreation provided site support at Refugio State Beach. This research was supported by the Minerals Management service, U.S. Department of the Interior, under mms agreement 14-35-01-00-CA-31063. The views and conclusions contained in this document are those of the authors and should not be interpreted as necessarily representing the official policies, either expressed or implied, of the U.S. Government. This paper is PISCO publication 138.

References

Atkinson, L. P., K. H. Brink, R. E. Davis, B. H. Jones, T. Paluszkiewicz, and D. W. Stuart (1986), Mesoscale hydrographic variability in the vicinity of Points Conception and Arguello during April–May 1983: The OPUS 1983 experiment, *J. Geophys. Res.*, *91*, 12,889–12,918.

Auad, G., and M. C. Henderschott (1997), The low-frequency transport in the Santa Barbara Channel: Description and forcing, *Cont. Shelf Res.*, *17*, 779–802.

Auad, G., M. C. Hendershott, and C. D. Winant (1999), Mass and heat balances in the Santa Barbara Channel: Estimation, description and forcing [Review], *Prog. Oceanogr.*, *43*, 111–155.

Barth, J. A., and K. H. Brink (1987), Shipboard acoustic Doppler profiler velocity observations near Point Conception: Spring 1983, *J. Geophys. Res.*, *92*, 3925–3943.

Battisti, D. S., and B. M. Hickey (1984), Application of remote wind-forced coastal trapped wave theory to the Oregon and Washington coasts, *J. Phys. Oceanogr.*, *14*, 887–903.

Beale, E. M. L., and R. J. A. Little (1975), Missing values in multivariate analysis, in *Computational Practice in Mathematical Programming*, 129–145 pp., Elsevier Sci., New York.

Brink, K. H. (1983), The near-surface dynamics of coaastal upwelling, *Prog. Oceanogr.*, *12*, 223–257.

Brink, K. H. (1991), Coastal-trapped waves and wind driven currents over the continental shelf, *Annu. Rev. Fluid Mech.*, *23*, 389–412.

Brink, K. H., and D. C. Chapman (1985), Programs for computing properties of coastal trapped waves and wind driven motions over the continental shelf and slope, report, Woods Hole Oceanogr. Inst., Woods Hole, Mass.

Brink, K. H., and R. D. Muench (1986), Circulation in the Point Conception-Santa Barbara Channel region, *J. Geophys. Res.*, *91*, 877–895.

Chen, C.-S., and D. P. Wang (1999), Data assimilation model study of the Santa Barbara Channel circulation, *J. Geophys. Res.*, *104*, 15,727–15,741.

Cho, K., R. O. Reid, and W. D. Nowlin (1998), Objectively mapped stream function fields on the Texas-Louisiana shelf based on 32 months of moorerd current meter data, *J. Geophys. Res.*, *103*, 10,377–10,390.

Davis, R. E., and P. Bogden (1989), Variability on the California Shelf forced by local and remote winds during the Coastal Ocean Dynamics Experiment, *J. Geophys. Res.*, *94*, 4763–4783.

Gurgel, K. W. (1994), Shipborne measurement of surface current fields by HF radar, *Onde Electr.*, *74*, 54–59.

Harms, S., and C. D. Winant (1998), Characteristic patterns of the circulation in the Santa Barbara Channel, *J. Geophys. Res.*, *103*, 3041–3065.

Hendershott, M. C., and C. D. Winant (1996), The circulation of the Santa Barbara Channel, *Oceanography*, *9*, 114–121.

Hickey, B. M. (1992), Circulation over the Santa Monica-San Pedro Basin and Shelf, *Prog. Oceanogr.*, *30*, 37–115.

Huyer, A. (1983), Coastal upwelling in the California current system, *Prog. Oceanogr.*, *12*, 259–284.

Jamshidian, M., and P. M. Bentler (1999), ML estimation of mean and covariance structures with missing data using complete data routines, *J. Educ. Behavioral Stat.*, *24*, 24–41.

Jamshidian, M., and R. J. Jennrich (1996), Acceleration of the EM algorithm by using quasi-Newton methods, *J. R. Stat. Soc.*, *59*, 569–587.

Kolpack, R. J. (1971), *Biological and Oceanographical Survey in the Santa Barbara Channel Oil Spill 1969–1970*, vol 2, 447 pp., Univ. of South. Calif., Los Angeles.

Miller, A. J., P. F. J. Lermusiaux, and P.-M. Poulain (1996), A topographic-Rossby mode resonance over the Iceland-Faroe Ridge, *J. Phys. Oceanogr.*, *26*, 2735–2747.

Nishimoto, M. M., and L. Washburn (2002), Patterns of coastal eddy circulation and abundance of pelagic juvenile fish in the Santa Barbara Channel, California, USA, *Mar. Ecol. Prog. Ser.*, *241*, 183–199.

Oey, L.-Y. (1999), A forcing mechanism for the poleward flow off the southern California coast, *J. Geophys. Res.*, *101*, 13,529–13,540.

Oey, L. Y., D. P. Wang, T. Hayward, C. Winant, and M. Hendershott (2001), "Upwelling" and "cyclonic" regimes of the near-surface circulation in the Santa Barbara Channel, *J. Geophys. Res.-Oceans*, *106*, 9213–9222.

Orchard, T., and M. A. Woodbury (1972), A missing information principle: Theory and applications, paper presented at 6th Berkekley Symposium on Mathematics, Statistics, and Probability, California.

Paduan, J. D., and L. K. Rosenfeld (1996), Remotely sensed surface currents in Monterey Bay from shore-based HF radar (Coastal Ocean Dynamics Application Radar), *J. Geophys. Res.*, *101*, 20,669–20,686.

Pedlosky, J. (1987), *Geophysical Fluid Dynamics*, Springer-Verlag, New York.

Pierini, S. (1996), Topographic Rossby modes in the Strait of Sicily, *J. Geophys. Res.*, *101*, 6429–6440.

Sverdrup, H. V. (1938), On the process of upwelling, *J. Mar. Res.*, *2*, 155–164.

Vastano, A. C., and R. O. Reid (1985), Sea surface topography estimation with infrared satellite imagery, *J. Atmos. Oceanic Technol.*, *2*, 393–400.

Wallace, J. M. (1972), Empirical orthogonal representation of time series in the frequency domain. part I Theoretical considerations, *J. Appl. Meteorol.*, *11*, 887–892.

Winant, C. D., R. C. Beardsley, and R. E. Davis (1987), Moored wind, temperature, and current observations made during Coastal Ocean Dynamics Experiments 1 and 2 over the northern California continental shelf and upper slope, *J. Geophys. Res.*, *92*, 1569–1604.

Winant, C. D., D. J. Alden, E. P. Dever, K. A. Edwards, and M. C. Henderschott (1999), Near-surface trajectories off central and southern California, *J. Geophys. Res.*, *104*, 15,713–15,726.

E. Beckenbach and L. Washburn, Institute for Computational Earth System Science, Department of Geography, University of California, Santa Barbara, Santa Barbara, CA 93106-3060, USA. (edwin@ices.ucsb.edu)